EXPECTATIONS FOR CRATER SIZE AND PHOTOMETRIC EVOLUTION FROM THE DEEP IMPACT COLLISION

PETER H. SCHULTZ*, CAROLYN M. ERNST and JENNIFER L. B. ANDERSON
Department of Geological Sciences, Brown University, Providence, RI 02912-1846, U.S.A.
*(*Author for correspondence; E-mail: peter_schultz@brown.edu)*

(Received 20 August 2004; Accepted in final form 10 January 2005)

Abstract. The NASA Discovery Deep Impact mission involves a unique experiment designed to excavate pristine materials from below the surface of comet. In July 2005, the Deep Impact (DI) spacecraft, will release a 360 kg probe that will collide with comet 9P/Tempel 1. This collision will excavate pristine materials from depth and produce a crater whose size and appearance will provide fundamental insights into the nature and physical properties of the upper 20 to 40 m. Laboratory impact experiments performed at the NASA Ames Vertical Gun Range at NASA Ames Research Center were designed to assess the range of possible outcomes for a wide range of target types and impact angles. Although all experiments were performed under terrestrial gravity, key scaling relations and processes allow first-order extrapolations to Tempel 1. If gravity-scaling relations apply (weakly bonded particulate near-surface), the DI impact could create a crater 70 m to 140 m in diameter, depending on the scaling relation applied. Smaller than expected craters can be attributed either to the effect of strength limiting crater growth or to collapse of an unstable (deep) transient crater as a result of very high porosity and compressibility. Larger then expected craters could indicate unusually low density ($<0.3\ \mathrm{g\,cm^{-3}}$) or backpressures from expanding vapor. Consequently, final crater size or depth may not uniquely establish the physical nature of the upper 20 m of the comet. But the observed ejecta curtain angles and crater morphology will help resolve this ambiguity. Moreover, the intensity and decay of the impact "flash" as observed from Earth, space probes, or the accompanying DI flyby instruments should provide critical data that will further resolve ambiguities.

Keywords: Deep Impact, porous targets, comets, oblique impact, NASA Ames Vertical Gun Range, laboratory experiments, Comet 9P/Tempel 1

1. Introduction

The NASA Discovery mission "Deep Impact" (DI) will guide a 360 kg (excluding propellant) probe into the path of Comet 9P/Tempel 1 in July 2005 with a net velocity of $\sim 10.2\ \mathrm{km\,s^{-1}}$. A companion spacecraft will capture the details of the collision process and resolve the resulting crater during a close approach of about 500 km (see A'Hearn *et al.*, this volume). One of the primary goals of this mission is to analyze spectroscopically pristine cometary materials excavated from below the surface. These materials will be observed in the ejecta plume during excavation and in the annulus of ejecta deposited around the final crater. Such a strategy may seem straightforward, but uncertainties in the actual nature of the upper 10 meters of the surface make specific *a priori* predictions difficult. The outcome of the collision

Space Science Reviews (2005) 117: 207–239
DOI: 10.1007/s11214-005-3383-7

will provide new constraints on the physical nature of the surface and subsurface while establishing a new benchmark for the cratering process.

The scientific basis for using an active probe to characterize subsurface materials of a planetary body dates back to the Ranger missions in the 1960's. In addition to the successful on-board cameras, attempts were made at the Jet Propulsion Laboratory (JPL) to view and calibrate these collisions on the Moon using earth-based telescopes. This concept received more serious study at JPL in 1993 when Marc Adams initiated an internally funded effort to assess possible measurements that could be made by hypervelocity impacts into planetary surfaces, e.g., a multiple asteroid mission. This effort resulted in a Director's Research and Development Fund proposed to JPL in 1995 with promising initial results (Schultz *et al*., 1996; Adams *et al*., 1997). Concurrently, JPL program managers excited by the concept actively solicited several possible mission scenarios from the community, including hypervelocity probes as part of possible missions to Europa and Pluto and multiple asteroid encounters. The Department of Defense (and several national laboratories) developed similar mission concepts, including the Clementine II mission, which would have involved impacting an asteroid. But in 1996, Alan Delamere and Mike Belton (with JPL, NOAO, and Ball Aerospace) developed the basis for the current Deep Impact mission concept with emphasis on exposing pristine materials from below the surface layer of a comet using a hypervelocity probe (see A'Hearn *et al.,* this volume). Consequently, the concept of kinetic probes for a planetary exploration has a rich scientific and engineering history, but NASA Discovery's Deep Impact mission is the first to be fully developed to flight status.

The effect of the DI impact on Tempel 1 can be assessed through theoretical calculations and laboratory experiments scaled up to conditions for the DI experiment. In both cases, the low surface gravity ($0.04\,\mathrm{cm\,s^{-2}}$) or unusual surface properties (low density) on Tempel 1 may result in surprises. At one extreme, the crater may be much smaller than expected due either to energy losses during the compression stage or to the effects of strength, both processes potentially contributing to little ejecta or surface expression (e.g., Housen *et al*., 1999). At the other extreme, a low-strength, porous particulate upper surface (>25 m) may result in a large crater limited in its lateral dimensions only by its meager surface gravity or the effects of deep penetration (e.g., Schultz, 2001; 2003a; Schultz *et al*., 2002). Because imaging sequences for DI require planning for the maximum crater size, initial estimates focused on direct extrapolations of gravity-controlled scaling relations for a loose particulate target (e.g., Schultz, 2001).

In order to be prepared for the event, a series of laboratory impact experiments are being performed at the NASA Ames Vertical Gun Range (AVGR). These experiments are designed to explore the effect of a wide range of target variables on crater evolution, final crater dimensions, and the photometry of the brief "flash" induced by the thermal plume. A range of possible target properties can be imagined. First,

physical reworking (due to volatile escape or regolith development) may result in a loose, porous surface of silicate/organic particulates. Second, cometary processes could produce a weakly bonded, highly porous surface layer. Third, volatile losses could create an indurated surface lag. These three extremes then could be extended to additional scenarios where the underlying substrates (including pristine volatiles) exist at depths from 1 m to 20 m.

The first three scenarios provide end-member properties that could dramatically affect the size of the crater and the amount of material exposed for remote analysis. For the purposes of discussion here, the first scenario will be called the porous regolith (PR) model; the second, the "under-dense regolith" (UR) model; and the third, the "strength-controlled" (SC) model. The fourth scenario will be collectively termed the "composite and layered" (CL) model.

The targets used in the experiments were not chosen to provide direct simulations of the DI crater. Rather, each target type provided different properties that would aid in relevant extrapolations. For example, carbonates do not represent cometary materials but impacts into carbonates result in strong atomic/molecular emissions with little thermal radiation. These spectra can be used to characterize the vapor plume at impact velocities available in laboratory experiments (Schultz, 1996; Sugita *et al*., 2003). Similarly, a thick, purely silicate surface layer is unlikely, but use of such a target in laboratory experiments establishes scaling relations and partitioning of kinetic into radiant energy for heated particulates. Moreover, the use of very different physical properties of the target material allows exploring a wide range of cratering outcomes.

Recent results from encounters with Comets Borelly (Soderblom *et al*., 2002) and Wild 2 (Brownlee *et al*., 2004) have provided unprecedented views of cometary surfaces at scales of 100 m's. It is the response of the surface and substrate at meter scales to the Deep Impact collision, however, that will affect what is observed. Consequently, the approach here is to consider a range of scenarios in order to assist in rapid interpretations of the observations soon after the event. Discussion first places the various crater-scaling regimes in a conceptual framework. It then considers the contrasting evolution of the ejecta plume. Next, expectations for the impact "flash" are reviewed. These various observations are then combined in order to anticipate diagnostic observations for understanding the nature of the upper surface layers of the comet.

The goal of this contribution is to clarify the range of possible outcomes from the DI collision. While the impactor properties are known, some impact parameters (impact angle, comet properties) are not. Impact angle with respect to the comet surface may range from 90° (vertical) to as low as 10° depending on the targeted region and local slope effects. As will be shown, interpretations will need to depend not only on the appearance of the final crater but also on the evolution of the initial radiant energy, early-time plume evolution, ejecta curtain appearance, and coma brightening created by the total ejected mass.

2. Crater Scaling

2.1. General Considerations

Various studies have assessed the effect of critical independent variables on crater size, particularly in particulate targets (e.g., Gault *et al*., 1975; Gault and Wedekind, 1977; Schmidt, 1977; Schmidt and Holsapple, 1982; Holsapple and Schmidt, 1982; Schultz and Gault, 1985a, b; Housen *et al*., 1999). Additionally, new diagnostic tools are being applied to the evolution of the ejecta and their relation to the cratering flow field (e.g., Cintala *et al*., 1999; Anderson *et al*., 2003, 2004).

Impacts into competent targets result in craters with diameter limited by material strength; hence, this is termed the strength-controlled crater-scaling regime (Gault and Wedekind, 1977; Schmidt, 1977). Impacts into loose particulate targets (e.g., PR models), however, grow "freely" until gravity prevents material from escaping the cavity. This is called the gravity-controlled crater-scaling regime (Post, 1974; Chabai, 1977; Gault and Wedekind, 1977; Schmidt, 1977).

A third regime has been proposed for under dense particulate targets (UR models). Experiments using highly compressible, porous targets (e.g., pumice dust) resulting in reduced cratering efficiencies (relative to sand) due to internal energy losses (e.g., Schultz and Gault, 1985a). Nevertheless, crater-scaling relations indicated gravity-controlled growth over a wide range of projectile sizes and velocities. Housen *et al*. (1999) found that energy losses in highly porous targets mixed with fine fly ash result in smaller craters due to significant compaction with minimal ejecta. Other studies showed, however, that hypervelocity impacts into highly porous targets result in deep penetration prior to complete transfer of energy and momentum (O'Keefe *et al*., 2002; Schultz *et al*., 2002; Schultz *et al*., 2003a). Computational codes (O'Keefe *et al*., 2002) demonstrated the deep penetration in under-dense targets until R-T instabilities disrupt the impactor during the earliest stages of cratering. Projectile disruption during penetration in porous targets is the rationale for using brittle Pyrex projectiles in laboratory experiments since this process has been shown to affect key crater-scaling exponents (e.g., Schultz and Gault, 1983, 1985b; Schultz, 1988). Laboratory experiments, however, also allow tracking the process beyond the penetration stage described by O'Keefe *et al*. (2002) and reveal that crater formation in loose particulates resembles a deeply buried explosion at late stages with significant amounts of ejecta launched at high angles (Schultz *et al*., 2002; Schultz, 2003a). The high-angle ejecta were observed to return to the crater, which subsequently collapsed to produce a much smaller final crater.

In the following discussion empirical scaling relations widely used to estimate crater dimensions are first reviewed. Second, the various cratering regimes are considered in the context of possible conditions for the DI collision, e.g., very low gravity and high porosity targets. Third, experimental design is used to illustrate some of the processes controlling phenomena associated with highly porous

and compressible targets. Our focus here is on the size of the crater and what observations could be used to interpret the observed crater size and plume evolution. Additional details concerning the evolution of the plume over much longer time scales (days) are deferred to other contributions and future work.

2.2. Scaling Relations

The following relation (see Schmidt and Holsapple, 1982; Holsapple and Schmidt, 1982) describes strength-controlled crater scaling:

$$\frac{M_c}{m_p} = k\pi_{_Y}^{-\beta} \tag{1}$$

where k is an empirical constant; M_c, the total displaced mass (deformation and ejecta) at the end of crater formation; and m_p, the original impactor mass. The term π_Y is given by the following:

$$\pi_Y = \frac{\delta_t v^2}{Y} \tag{2}$$

where δ_t is the target density; v the impactor velocity; and Y the target strength. The exponent β depends on the controlling cratering process. For momentum-controlled cratering $\beta = 2$; for energy-controlled scaling, $\beta = 1$.

By contrast, gravity-controlled cratering is controlled by outward material flow field accelerated behind the shock front and is redirected by rarefactions off the free surface (Gault *et al*., 1968; Gault *et al*., 1975). This flow continues provided that it has sufficient velocity to escape the cavity. When ejecta velocities no longer allow escape from the cavity, then the following relation applies for the transient crater (maximum displacement prior to collapse):

$$\frac{M_c}{m_p} = k\pi_2^{-\alpha} \tag{3}$$

where π_2 is an inverse Froude number that scales inertial to gravitational forces (Chabai, 1977; Schmidt, 1977; Gault and Wedekind, 1977):

$$\pi_2 = 3.22\left(\frac{gr}{v^2}\right) \tag{4}$$

where r is the projectile radius; g the gravitational acceleration at the surface; and v the vertical velocity component represented by $v \sin\theta$ (Gault and Wedekind, 1977; Chapman and McKinnon, 1986; Schultz and Gault, 1990).

As recognized in experiments (Stöffler *et al*., 1975) and computations (e.g., Schultz *et al*., 1981), the total displaced mass is about twice the mass of the ejecta actually launched out of the crater. The amount of ejecta is important for the DI mission since it will control the over-all coma brightening following the impact as the total ejected mass (gas and dust) greatly exceeds the nominal daily flux. The

total displaced mass is important because it determines the final crater dimensions to be observed during the flyby.

The final diameter and depth for simple (un-collapsed) craters are commonly assumed to form a constant ratio, i.e., the crater diameter and depth are proportional. If the crater diameter is referenced to the pre-impact surface, it is termed the "apparent crater," and this aspect ratio ranges from 3:1 for strength-controlled metals (matched projectile/targets) to 4:1 for gravity-controlled particulate targets. Projectile aspect ratio, strain-rate effects, grain size (relative to the projectile), projectile failure, and projectile/target density also appear to affect scaling (e.g., Schultz, 1988). The transient crater diameter and depth, however, do not grow proportionally with each other. Laboratory and computational experiments demonstrate that crater depth reaches its maximum prior to crater diameter (Schultz *et al.*, 1981; Schultz, 1988). Consequently, non-proportional crater growth can result in pre-collapse crater aspect ratios very different from the nominal values depending on the effect of gravity, density contrast, and compressibility as will be discussed.

The independent variables for the impactor (the DI probe) are known, excepting the impact angle. The independent variables for the comet, however, are unknown or poorly constrained, including the strength, physical structure (layering), and the density. Consequently, these are the important variables to be explored through experiments. For the DI impact, the relative encounter velocity will ensure eventual catastrophic failure of the projectile at impact, even for the most extreme scenario of an under-dense surface layer. Consequently, Pyrex spheres are used in the laboratory experiments here as a more relevant analog for higher velocity impacts, including the DI impactor. Although composed of copper, holes in the DI impactor and the attached structures reduce the effective bulk density to about $1\,\mathrm{g\,cm^{-3}}$; consequently, Pyrex also provides reasonable density match.

The maximum transient crater diameter, D, for a gravity-controlled crater scaled to the projectile diameter, a, is given by (again following Holsapple and Schmidt, 1982):

$$\frac{D}{a} = k'\left(\frac{\delta_p}{\delta_t}\right)^{1/3}\left(3.22\frac{gr}{v^2}\right)^{-\alpha/3}. \tag{5}$$

The exponent α for particulate targets typically ranges from 0.48 to 0.56, depending on specific material properties and whether energy or momentum transfer dominates. Consequently, Equation (5) shows that direct extrapolations can become problematic when considering large sizes or extreme gravitational accelerations at the surface (Schmidt and Holsapple, 1982; Gault and Wedekind, 1977; Schultz, 1992).

Crater depth can be simply calculated by assuming a fraction of the final crater diameter. Experiments, however, reveal that crater depth can be arrested by a competent substrate at depth without significantly affecting the diameter, provided that the depth of the layer is greater than about three times the impactor diameter in the case of vertical impacts (Schultz, 2003b). Conversely, an under-dense target will

allow the projectile to penetrate deeply before termination. In this case, sufficient strength near the surface (or a weakly coupled shock at first contact) can result in an initially small diameter but deep crater. Unless allowed to grow to large diameter, this profile is unstable and collapses. Consequently, the strategy to watch the crater grow during the DI encounter (and the evolution of the ejecta plume and curtain) may prove as important as measurements of the final crater dimensions.

The density of the comet plays three roles. First, the bulk density and radius affect gravitational acceleration forces at the surface. Second, the near-surface density affects the amount of material (mass) displaced, i.e., crater size. Third, an underdense target may result in a weakly coupled shock near the surface, thereby resulting either in deep penetration of the projectile prior to transferring its momentum and energy or in compression effects with little excavation. The first two roles are readily incorporated into Equation (5). The last role is best appreciated in the context of the decay of peak pressure in relation to strength, gravity, and the initial stages of coupling.

Figure 1 illustrates the various cratering regimes expressed in terms of the peak pressure decay in the target. This graphical representation is based on theoretical considerations consistent with observations from experiments and computational

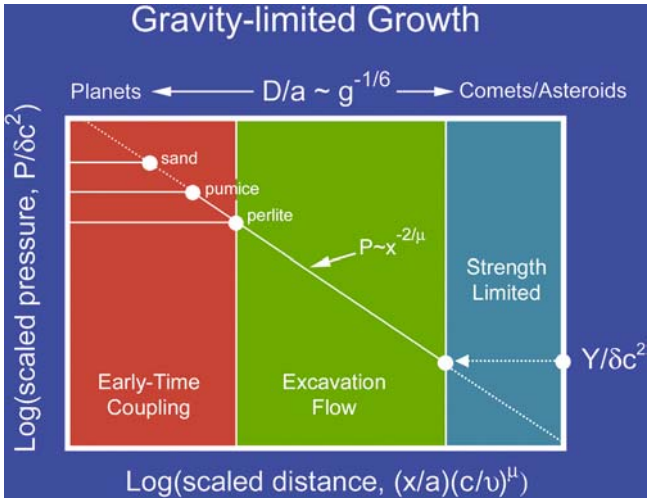

Figure 1. Schematic plot showing the stages of cratering in terms of scaled peak pressure decay as a function of scaled distance from impact (following Holsapple, 1987). Peak pressure is scaled to target density (δ) and sound speed (c); distance (x) is scaled by impactor diameter (a), velocity (v), and target sound speed. Different initial conditions during the compression stage eventually converge on a common pressure-decay relation at different scaled distances. The "excavation stage" occurs in the rarefaction zone behind the shock front. The limit of excavation is represented by two conditions. Strength-controlled craters are prevented from growing further when the peak pressures approach the strength limit (Y) as indicated by the lower axis. Gravity-controlled craters are limited by the ballistic excavation (upper axis) as described in the text.

codes (Holsapple, 1987). Immediately after impact, the impactor transfers its energy and momentum to the target. The transfer of energy and momentum is generally complete (coupled to the target) after the shock front has passed through the projectile to its back surface (Gault *et al.*, 1968). As a result, the stage of crater growth (i.e., distance, x, or depth, d at a given time) needs to be scaled to either a final crater dimension (e.g., radius, R) or to the projectile diameter. Alternatively, stage of growth can be represented in terms of time (t) relative to the total crater formation time or the length of time for the projectile to travel its diameter (i.e., the penetration time scale, a/v, along its trajectory):

$$\tau = \frac{t}{(a/v)} \tag{6}$$

where v is the impact velocity.

As recognized early in the study of cratering (e.g., Dienes and Walsh, 1970; O'Keefe and Ahrens, 1977), peak pressures eventually decay to a common material-dependent relationship after a sufficient time or distance from the impact. This far-field equivalence can be expressed in a useful description based on dimensional analysis for peak pressure (P) scaled to the target density (δ_t) and ambient sound speed (c) in the target:

$$\frac{P}{\delta_t c^2} = \left[\left(\frac{x}{a}\right)\left(\frac{c}{v}\right)^{\mu}\right]^{-2/\mu} \tag{7}$$

where μ is a pressure-decay exponent that depends on which coupling process dominates cratering. If cratering is controlled by momentum, then $\mu = 2/3$; if controlled by energy, $\mu = 1/3$ (Holsapple, 1987). At large distances from the source, however, the exponent $(2/\mu)$ approaches 2 in order to conserve momentum in the shock (see Dahl and Schultz, 1999, 2001). Lower values of μ (momentum scaling) also apply to porous particulate targets (Holsapple, 1987).

Equation (7) is useful for visualizing the effect of controlling variables on crater size relevant to the DI experiment. If strength-controlled, the crater can grow until the material strength exceeds the peak pressure. In competent targets, this represents the yield strength (ductile) or tensile (brittle) strength. Consequently (x/a) simply approaches (D/a) at the end of excavation (the lower abscissa in Figure 1). In reality, the decay slope also depends on target porosity, but this is ignored for purposes of illustration. At the other extreme, a completely strengthless target will permit the crater to grow until gravity no longer allows material to escape the cavity (upper abscissa). Under high gravity, the cavity becomes smaller for a given projectile size. Under very low gravity, the cavity grows until ejecta velocities are insufficient to achieve a ballistic range beyond the crater rim.

Because most materials exhibit some form of strength (e.g., cohesion), crater growth ceases when the peak pressure in the shock front no longer exceeds the scaled material strength ($Y/\delta_t c^2$ in Figure 1). Powdered pumice exhibits a high angle of friction under static conditions as demonstrated by its ability to form a

vertical face due to the irregular shapes of the constituent grains. Hypervelocity impact experiments into pumice powder demonstrate, however, that gravity controls excavation. This paradox is readily explained by the fact that excavation occurs under extension in the rarefaction zone behind the shock front (Gault *et al*., 1968). For example, a post-shock zone of distended powder ("bulking") is observed well beyond the rim of craters produced in pumice. Consequently, the relevant strength term for particulate targets is not simply the static strength but the resistance (frictional shear) during dynamic flow in the rarefaction wave behind the shock front. In laboratory experiments, the gravity-controlled crater is much smaller than the disturbed annulus beyond the rim. But under very low gravity, it is likely that the resistance to flow will arrest the crater before it reaches its gravity limit. In Figure 1, the dashed horizontal line represents $Y/\delta_t c^2$ corresponding to this limit.

Compression primarily affects the initial stages of cratering rather than the final stages, as in gravity- and strength-controlled growth (Figure 1). As shown by O'Keefe and Ahrens (1977), different initial conditions eventually follow a single decay curve reflecting material properties behind the shock front. They converge at a distance approximately where the projectile detaches from the shock to the left in Figure 1. Within this zone, early-stage coupling (such as compression) is thought to be unimportant for later stage excavation flow, according to point-source theory (Holsapple and Schmidt, 1982, 1987). If experiments are performed under high gravity for a given target material (or for larger impactor size at a given gravity), then the gravity-controlled limit in the excavation flow regime will move to the left in this diagram (abscissa above) and shut down growth. For highly compressible targets under very high gravity, the cratering limit may overlap with the early-stage coupling.

The DI crater will form under very low gravity (from 0.04 cm s^{-2} to 0.08 cm s^{-2}). Consequently, the relevant issue here is the possible effect of unusual cometary materials resulting in significant internal energy losses at the outset (compression effects) such that the early-time compression zone consumes more of the excavation flow (to the right). The excavation limit is ultimately controlled either by the peak pressure relative to the material strength or by gravitational acceleration.

This general discussion relating input to output allows understanding the wide range of possible outcomes due to material properties of Tempel 1, including substrates with very low density, high porosity, and high compressibility as considered next.

2.3. Under-Dense, Porous Targets (PR Models)

There is a physical difference between the bulk target density (porosity) and compressibility. A highly porous target with a low bulk density can be relatively incompressible under static conditions. For example, particulate targets composed of hollow ceramic microspheres can be compressed to maximum packing with

considerable bulk compressive strength. Particulate pumice, vermiculite, and perlite targets represent the other end member where each constituent particle is highly compressible even after achieving maximum packing.

Experimental data reveal that even large projectile/target density ratios (>10) for incompressible, highly porous targets do not significantly affect crater scaling for gravity-controlled growth (Schultz and Gault, 1985a). Experiments using targets composed of hollow microspheres (bulk $\delta_t = 0.09\,\mathrm{g\,cm^{-3}}$; porosity $\sim$ 90%) and vermiculite (bulk $\delta_t = 0.09\,\mathrm{g\,cm^{-3}}$; porosity $\sim$ 90%) resulted in enormous transient craters consistent with expectations from Equation (5). Craters produced in targets composed of microspheres collapse due to the unstable crater profile, whereas craters in vermiculite retain their profile (see Figure 2).

Target density (porosity), however, does affect the peak pressure and its decay rate through the target. Consequently, experiments also were performed with different degrees of compaction of pumice powder: compressed ($1.5\,\mathrm{g\,cm^{-3}}$; porosity of 35%); uncompressed ($1.3\,\mathrm{g\,cm^{-3}}$; porosity of 43%); and lightly fluffed ($1.1\,\mathrm{g\,cm^{-3}}$; porosity $\sim$ 50%). The compressibility of these targets can be illustrated by low-velocity, free-fall experiments. A solid rod dropped from 0.5 m will penetrate completely through to the bottom of the target container (below the crater floor) for the fluffed pumice target. Hypervelocity impacts ($>5\,\mathrm{km\,s^{-1}}$) by Pyrex or aluminum

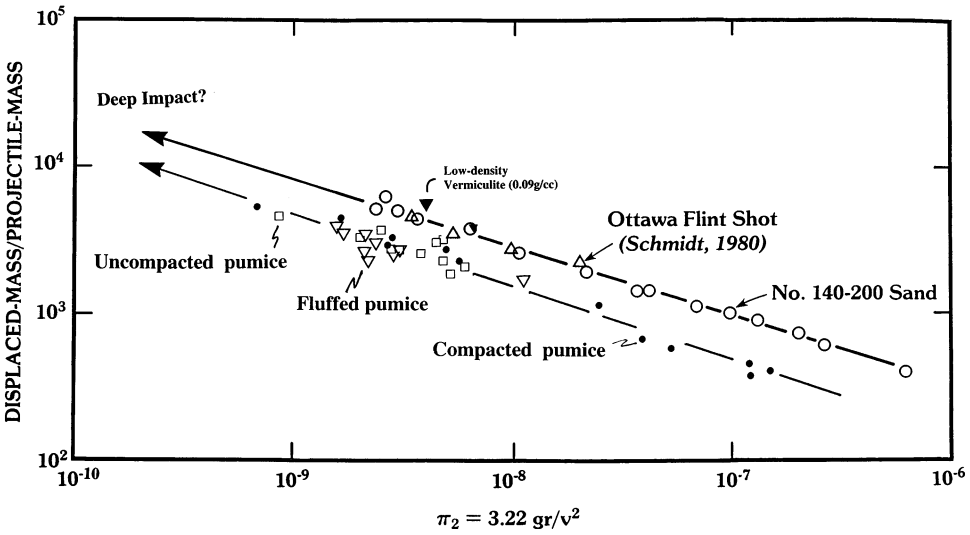

Figure 2. Cratering efficiencies (total mass displaced relative to the impactor mass) plotted against the gravity-scaling parameter (π_2) expressed in terms of the impactor radius (r), gravitational acceleration (g), and impactor velocity (v). Data include craters produced in No. 140–200 μm sand (Schultz and Gault, 1985a), Ottawa flint shot (Schmidt, 1980), and compressible targets (pumice, vermiculite). Three types of pumice with different bulk densities are shown: compacted, uncompacted, and fluffed. The lower cratering efficiency for pumice is attributed to internal energy losses during the early stages of compression.

(or even copper) into sand or pumice, however, do not penetrate below the crater floor throughout crater growth due to the role of shock disruption of the projectile. Figure 2 summarizes cratering efficiencies for a wide range of targets with different densities. These experiments indicate that impactor/target density ratios, target porosity (<50%), and cohesion all have little effect on crater scaling of loose particulates at 1 g over the range of variables in use.

2.4. Under-Dense, Compressible Targets (UR Models)

Perlite targets provide a useful surrogate to assess the consequences of both high bulk porosity and high compressibility of constituent particles (Housen *et al.*, 1999). The experiments for the present study included targets of perlite granules (composed of a highly porous silicate) sieved to retain grains smaller than 1 mm (bulk $\delta_t = 0.20\,\mathrm{g\,cm^{-3}}$). In contrast with the experiments by Housen *et al.* (1999), additives such as fly ash were not included because such fine-grained components can introduce viscous drag that can dominate the process, especially at low impact velocities ($<2\,\mathrm{km\,s^{-1}}$). Such experimental conditions also can complicate the distinction between early-stage compression effects (and poor shock coupling) and late-stage strength limits (Figure 1).

Cratering efficiency for impacts into sieved perlite increases with decreasing impact angle (referenced to the horizontal) as shown in Figure 3, directly opposite to well-coupled impacts into sand and pumice (Gault and Wedekind, 1978). "Quarter-space" experiments reveal the evolution of crater growth and expose the underlying cause for this counter-intuitive result. In this approach, the projectile is aimed at the surface directly adjacent to a plexiglass sheet, thereby allowing observations of crater growth using high-speed imaging. Such an approach has been used in numerous investigations (e.g., Piekutowski, 1977; Schmidt and Housen, 1987). The evolution of the transient crater for the sieved-perlite experiments is shown in Figure 4. In vertical impacts, the projectile penetrates deeply before outward (lateral) growth occurs (Figure 4a). Because of the unstable transient crater shape under 1 g, the final crater collapses and becomes much smaller. At slightly oblique impact angles (Figure 4b) the initial penetration funnel eventually opens to produce a large transient crater below the surface. As impact angle decreases still further (15–30°), the crater becomes stable and cratering efficiency actually increases relative to expectations (Figure 4c) as demonstrated in Figure 3.

The difference between the transient and final crater shape is shown in Figure 5 for different particulate targets. The diameter-to-depth aspect ratio (x/d) evolves from 0.5 within the first 4 ms to 1.5 at the end of excavation in the quarter-space experiments. In contrast, the final D/d value for nominal (half-space) experiments with perlite is almost 3. Consequently, crater growth for both vertical and oblique impacts into sieved perlite targets is non-proportional throughout most of crater growth and results in an unusual aspect ratio for the pre-collapse transient crater.

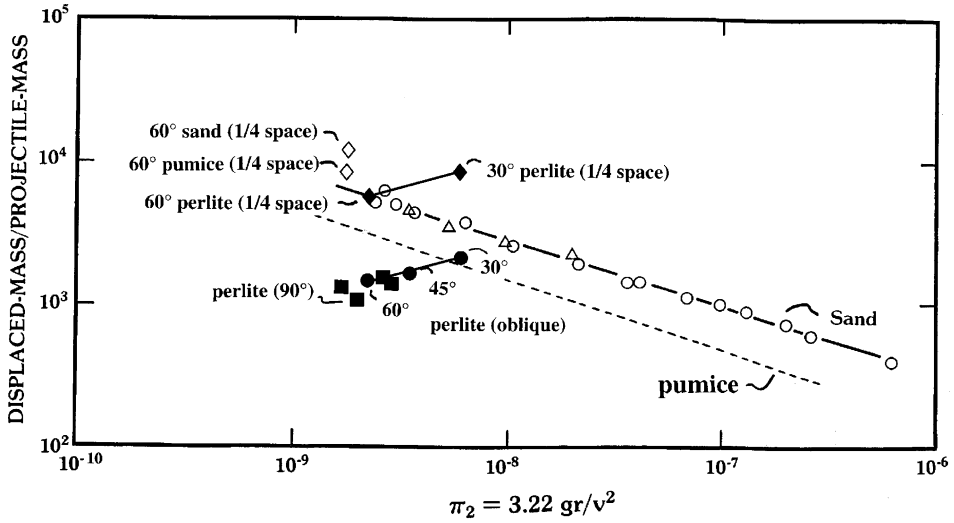

Figure 3. Cratering efficiencies for under-dense (sieved perlite) targets in contrast with results for sand and pumice targets. Final craters produced in perlite by vertical impacts (solid squares) are much less efficient than the final craters produced in pumice (dashed line, see Figure 2) and sand. Oblique impacts into perlite (solid circles) become progressively more efficient with decreasing impact angle, in contrast with impacts into denser particulate targets (pumice and sand). Transient craters measured from quarter-space experiments (open diamonds for 60° impacts into pumice and sand) reveal that cratering efficiencies prior to collapse of the cavity are generally consistent with expectations for the appropriate target (but slightly enhanced due to the quarter-space design). Oblique impacts (30°) into perlite using the quarter-space design (solid diamond), however, resulted in greater cratering efficiencies due to shallower depths of energy/momentum transfer.

Such results indicate that the underlying controlling process for under-dense, highly compressible targets is the effective penetration depth where the impactor energy and momentum are fully transferred to the target. This process is illustrated for the earliest stages of cratering using quarter-space experiments (Figure 6). Figure 6a provides a reference for a 60° impact into sand. Vertical (Figure 6b) and near-vertical (Figure 6c) impactors into perlite disappear in a long penetration funnel beneath the surface similar to early-time computational results of O'Keefe *et al.* (2002). The deep penetration in both cases results in a crater formed by a process resembling a deeply buried explosion. In contrast, a low-angle impact (30°) into perlite (Figure 6d) couples at a more optimum depth for both maximum cratering efficiency and stable final crater shape. The late-stage transient craters are shown in Figure 7.

The laboratory experiments used weak impactors (Pyrex) that totally disrupt at impact, even in the low-density perlite. Disruption also should occur for the 10.2 km s^{-1} DI collision, even for extremely low densities of the comet surface materials. This is a major difference between impact experiments that do and do not have sufficient velocity to exceed the sound speed and failure limit in both target and projectile, especially for under-dense targets.

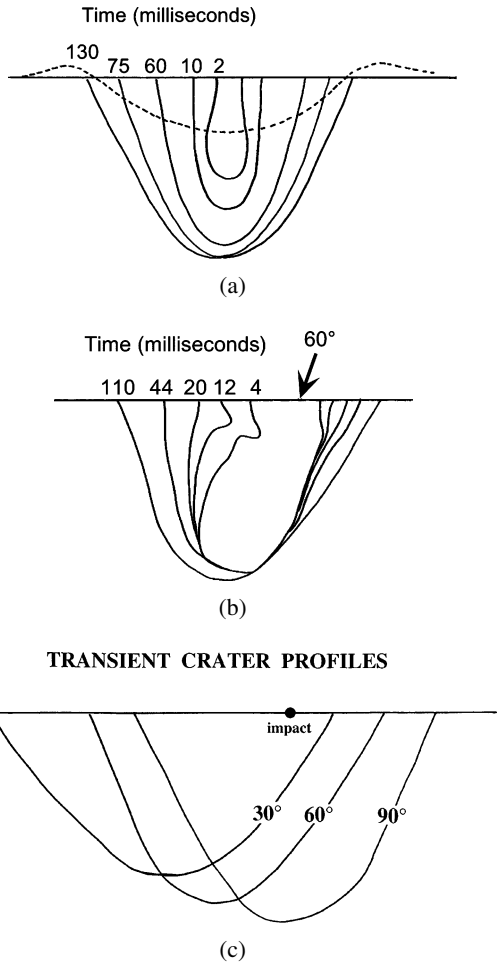

Figure 4. (a) Crater evolution for vertical hypervelocity ($\sim$6 km s^{-1}) impact by a 0.318 cm diameter pyrex sphere into sieved perlite using the quarter-space experimental design. An early-stage penetration funnel eventually expands into a deep paraboloid. The final crater (dashed line) is much smaller than the transient crater (at 130 ms) due to crater collapse and the return of high-angle ballistic ejecta to the cavity. (b) Crater evolution for an oblique (60°) hypervelocity (5.6 km s^{-1}) impact by a 0.318 cm diameter Pyrex sphere into sieved perlite revealed by quarter-space design. The initial penetration funnel eventually opens ("blooms") to produce a large transient crater before collapsing. (c) Comparison of maximum transient crater profiles for different-angle impacts into perlite for the same impact velocity and projectile size. Immediately after formation, transient craters collapse.

The quarter-space experiments specifically reveal four material displacement regimes that evolve during hypervelocity impacts (e.g., see Figures 4–7). A penetration funnel characterizes the first regime at early times as target material is compressed in front of the fragmenting projectile. This funnel expands cylindrically, similar to the mach tube creating during hypervelocity atmospheric entry (e.g.,

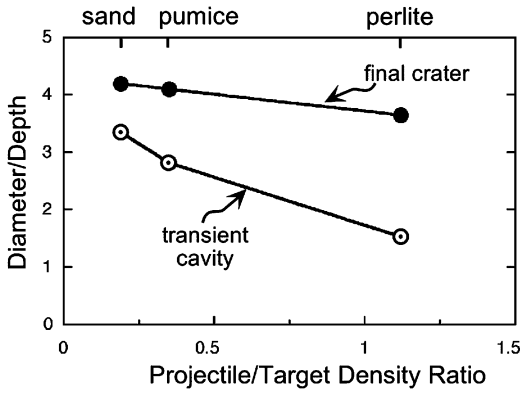

Figure 5. Effect of projectile/target density ratio on the crater aspect ratio (diameter/depth) for final (half-space target) and transient (quarter-space target) craters. Data are for hypervelocity (6 km s^{-1}) impacts at 60° from the horizontal.

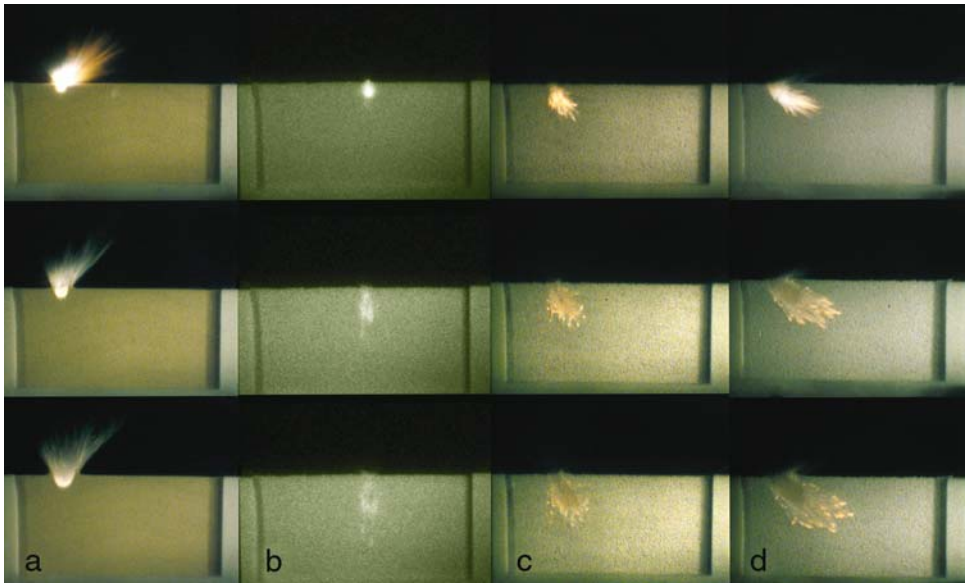

Figure 6. Comparison of initial energy/momentum-transfer process revealed in quarter-space experiments using high-speed imaging (0.17 ms inter-frame time). High-angle (60°) impact into sand (a) produces an exposed flash and growing cavity lined with incandescent material over the first 0.5 ms. Vertical (90°) impact into sieved perlite (b) produces a hidden flash within a deep penetration funnel that later opens into a large transient crater (see Figure 4a). High-angle (60°) impact into sieved perlite catastrophically disrupts the pyrex sphere into fragments that disperse ahead of the penetration funnel and the subsequent cavity (c). Low-angle impact (30°) disperses melt target/projectile fragments at a shallow depth and produces a much larger maximum transient crater (d) as documented in Figure 3.

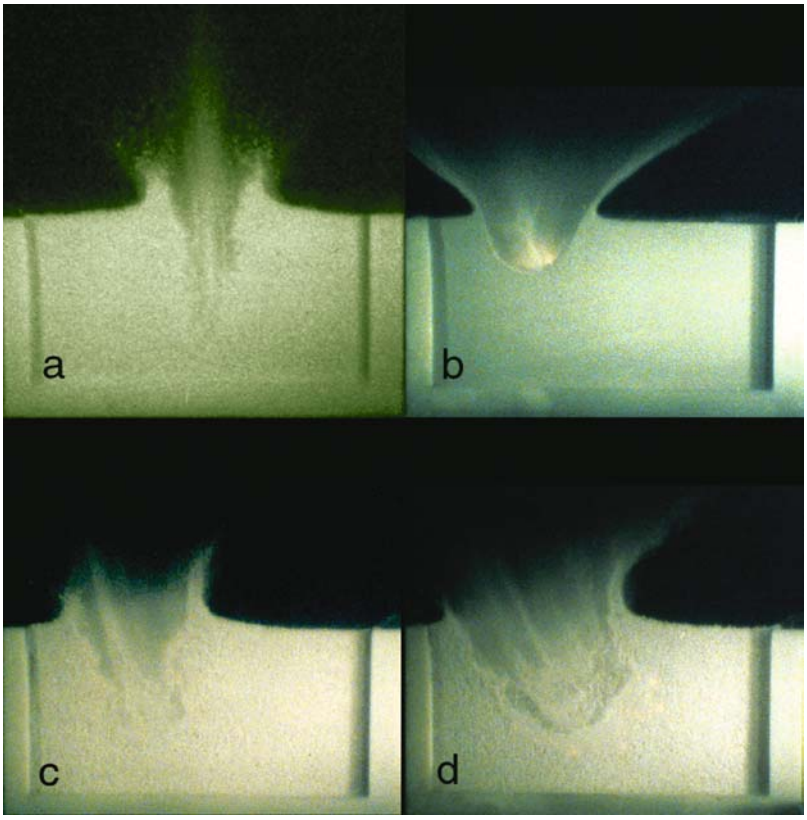

Figure 7. Late-stage (100 ms) transient craters for a vertical impact into perlite (a); high-angle (60°) impact into sand (b) and sieved perlite (c); and low-angle (30°) impact into sieved perlite (d).

Boslough *et al*., 1994). In under-dense targets, the explosively disrupted/melted fragments continue into the target ahead of the funnel. In sand targets, these fragments line the growing cavity. The second stage of displacement is represented by high-angle (>80°) ejecta. Such high ejection angles develop as the result of an expanding cavity at depth, analogous to a deeply buried explosive charge. A pillar-like plume of high-angle ballistic ejecta characterizes the third stage and lasts throughout crater formation. This stage represents the combined effects of cavitation (inward flow) and escape. Highly directed vapor plumes also have been observed during hypervelocity impacts into dry ice targets (Schultz, 1996). The fourth stage is an outward-moving ejecta curtain in response to rarefaction-deflected excavation flow from the free surface as witnessed in experiments using sand targets (Figure 7b).

The collision of Comet Shoemaker-Levy with the atmosphere of Jupiter may provide an end-member case for a low-density projectile into a very low-density target at a much higher velocity (e.g., see Boslough *et al*., 1994). This was not a solid-surface impact, and a final crater (and ejecta from the surface) did not form.

Nevertheless, ejecta (from the impactor) did produce a high-angle reverse plume similar to the early-time results shown in Figure 6 due to the deep penetration prior to fully coupling its energy.

3. Possible Crater Dimensions for the Deep Impact Crater

Can gravity scaling observed in the laboratory be extended to Tempel 1? This question may not be answered until 2005 when such an experiment finally will be made during the DI collision. Nevertheless, small bowl-shaped craters exist on Mathilde and generally resemble lunar craters formed in a thick regolith. Blocks and boulders around these craters also could be breccias created by compressed regolith materials. Impact experiments using sand do not generate such products, whereas impacts into pumice do create compressed sediments and melt products comparable in size to the projectile due to the lower melting temperature of the constituent grains.

One of the more critical unknowns will be the nature of the transmission of the compression wave through a highly porous regolith. If an AVGR experiment could be done under the same gravity as on Tempel 1 ($0.04\,\mathrm{cm\,s^{-2}}$), the crater rim would extend almost 7 times farther with the peak pressure reduced by a factor of 50 (depending on the value of $2/\mu$ in Equation (7)) with the terminal ballistic ejection velocity approaching $10\,\mathrm{cm\,s^{-1}}$ (versus $50\,\mathrm{cm\,s^{-1}}$at 1 g). Late-stage material motions observed in quarter-space experiments approach this velocity within the target but only contribute to rim uplift prior to collapse (rather than ejecta beyond the rim).

Table I provides summaries of expectations for gravity-controlled growth (Equation (5)) for different target densities extrapolated to a value of π_2 for the Deep Impact collision. Table II provides empirically derived values for the corresponding

TABLE I

Different materials (Extrapolated to Deep Impact).

	Target density $0.3\,\mathrm{g\,cm^{-3}}$		Target density $1.0\,\mathrm{g\,cm^{-3}}$	
	Size	Formation times	Size	Formation times
Pumice	$D_a = 89$ m	225	62 m	190
	$d_a = 22$ m		15 m	
Sand #140–200	$D_a = 141$ m	280	94 m	230
	$d_a = 35$ m		24 m	
Sand #140–200 (compression)	$D_a = 111$ m	250	74 m	205
	$d_a = 28$ m		19 m	
Sand (energy scaling)	$D_a = 238$ m	370	160 m	300
	$d_a = 60$ m		40 m	

TABLE II
Values of empirically derived constants and exponents.

	k	k'	$\propto$
Pumice	0.0963	0.756	0.518
Loose sand	0.240	1.30	0.51
Sand (compressible)	0.120	1.03	0.51
Sand (energy scaling)	0.0029	0.273	0.75

constants and exponents. These expectations provide maximum diameters and depths for proportional growth based on experiments as benchmarks. If the bulk density of the comet (and the impacted surface) is overestimated by a factor of two, the predicted crater diameter would be decreased by about 15%. The predicted crater-formation time (in seconds) for the craters in Table I could range from 200 to ~400 s if this regime applies. Three results for sand targets are shown. The first estimate directly extrapolates the experimental results. The second assumes that energy losses due to compaction reduce cratering efficiency at the outset but not the exponent α. The third estimate considers the possibility that energy scaling controls cratering efficiency with an exponent of $\alpha \sim 0.75$ (pure energy scaling). Energy scaling may apply when impact velocities greatly exceed the sound speed in the projectile, as well as in the target (Gault and Wedekind, 1977; Schultz and Gault, 1983; Schultz, 1988). Under these conditions, energy coupling occurs soon after first contact.

Both strength-controlled (late stage) and compression-dominated (early stage) effects may produce small craters close to the resolution limit of the DI high-resolution instrument (HRI). As discussed below, however, those two extremes can be distinguished by the nature of the ejecta plume (photometry and shape), in addition to the final crater morphology. The extrapolations shown in Table I assume proportional growth, but various late-stage hydrocode models (e.g., Orphal, 1977; Schultz *et al.*, 1981) and experiments (e.g., Figures 4–7) indicate that craters reach their maximum crater depth before growing laterally. Consequently, a purely gravity-controlled crater produced on Tempel 1 should be shallower than craters observed in 1-g laboratory experiments, even without the effects of a stratified target. But if a regolith-covered substrate exists (CL model), it likely would produce one of the distinctive morphologies observed in small lunar craters (e.g., Quaide and Oberbeck, 1968). Experiments indicate that the gravity-controlled crater diameter is not appreciably affected for a surface layer depth three times the projectile diameter since the lateral shock would have been fully coupled (Schultz, 2000). In the inverse case (indurated surface over a porous substrate), experiments demonstrate the formation of large spall plates (Gault *et al.*, 1968).

In a completely strengthless target, crater scaling should follow predictions, but any residual post-shock target strength at very large distances from the impact point

would reduce these predictions. Conversely, rapid vapor expansion by volatiles in Tempel 1 also could result in backpressures (or exothermic release from chemical reactions) that might offset the effects of strength. Hypervelocity impact experiments using dry ice at the impact point have been observed to augment cratering efficiency at 1 g. In this case, vapor driven downward into the cavity creates a backpressure that boosts crater growth in strengthless or low-strength targets.

4. Crater and Ejecta Evolution

Witnessing crater formation on comet Tempel 1 will help constrain conflicting interpretations based only on the final morphology. Even though the crater will not be resolved at impact, the ejecta curtain profile will be imaged either directly or indirectly through its shadow crossing the cometary surface. Four observables will assist in interpretations: initial photometric evolution, shape and expansion of the ejecta curtain, opacity of the curtain during formation, and the total coma brightening due to the sudden addition of gas and dust to the coma.

First, photometry of the initial thermal plume will depend on the composition, porosity and structure of the target. Ongoing experiments are assessing these effects (Ernst and Schultz, 2002–2004) and initial results are described in the following section. Thermal radiation, however, will only partly control the light output. Strong aluminum oxide molecular bands due to reactions between the aluminum within the impactor ($\sim$6%) and cometary oxygen also may enhance peak intensity in the visible (as noted in laboratory experiments).

Second, the shape and expansion rate of the ejecta curtain (directly or through its shadow on the surface) will provide an indirect measure of crater growth (Figure 8). The advance of the ejecta curtain (speed and diameter at a given time) across the

---

Figure 8. Sequence showing ejecta evolution for a 60° impact at $\sim$5 km s^{-1} (0.635 cm diameter Pyrex sphere) into pumice covered by a thin layer of red dry paint powder. First frame (at impact) shows the rapidly expanding vapor and plasma plume directed downrange (to the left), followed by a conical curtain of incandescent ejecta (next 5 frames or $\sim$0.93 ms). After the fifth frame, the sequence is shown every 50 ms. A high-angle plume (directed back toward the initial trajectory) develops during the earliest stages but is surrounded by an annulus that expands across the surface after crater formation as ballistic ejecta within the curtain strike the surface. After crater formation, the curtain speeds up since it is composed of progressively faster ballistic ejecta.

Figure 11. Ejecta velocity vectors within a thin laser sheet cutting through the ejecta curtain $\sim$8 cm above the target surface at a given time. The laser sheet illuminates individual ejecta particles and an algorithm allows deriving the velocity vectors shown. Vertical impacts into loose sand (a) show that the flow-field is very well defined and symmetrical: ejecta crossing the laser plane occur in a narrow ring ejecta velocities are all very similar at a given time. A vertical impact into sieved perlite (b) shows a similar pattern (with slightly higher ejecta angle) but appears to be split. Very fine-grained powder in a vertical plume (see Figure 7a) blocks the laser used in the technique (see Anderson *et al.*, 2004) and produces the gap in velocity vectors in Figure 11b.

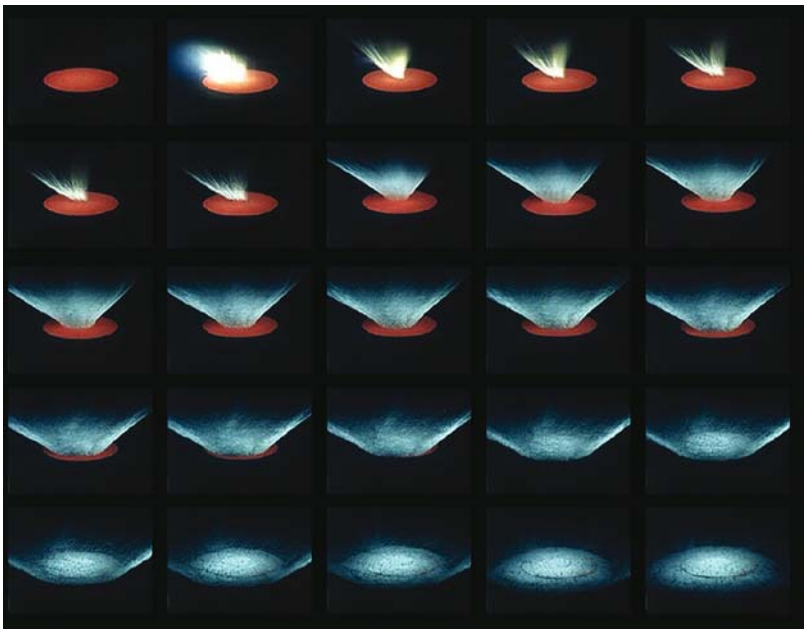

Figure 8.

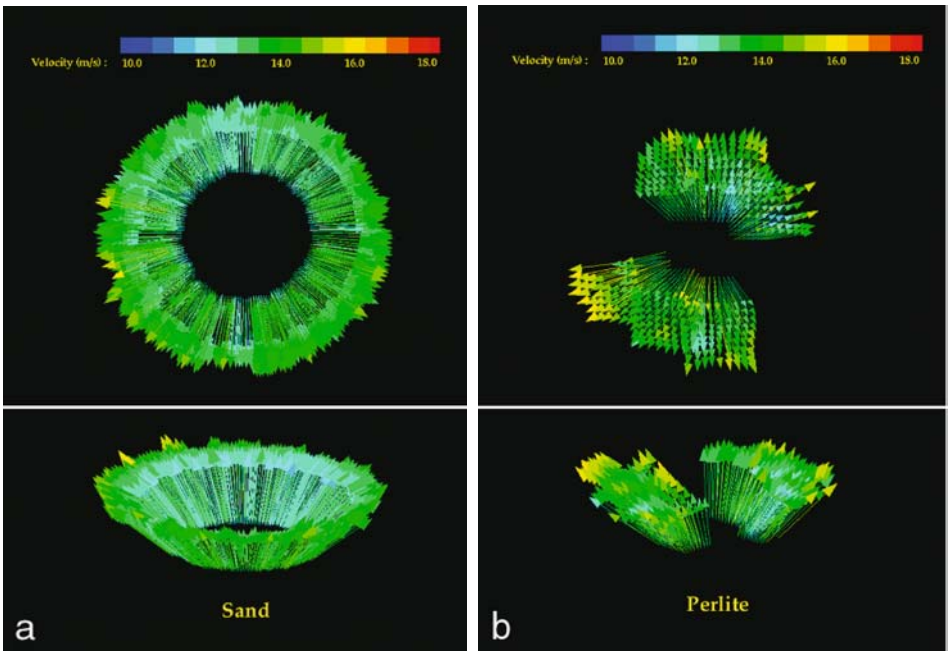

Figure 11.

surface provides a measure of the appropriate controlling variable, i.e., gravity or strength. If gravity constrains the maximum crater diameter, then empirically derived scaling equations can be used (e.g., Housen *et al*., 1983; Anderson *et al*., 2003, 2004) for extrapolation to the DI impact. More recent analyses reveal that such scaling equations depend on projectile/target density contrast and impact angle (e.g., Anderson *et al*., 2003, 2004). At late stages of growth (>50%) the following scaling relation applies for fine-grained sand targets:

$$\upsilon_e = \kappa(gR)^{1/2}\left(\frac{x}{R}\right)^{-w} \tag{8}$$

In Equation (8), κ and w are empirically derived values; R is the final apparent crater radius; and x is the radius of crater at time of ejection. Point source models (Housen *et al*., 1983) predict that the exponent will depend the coupling process (energy or momentum) at impact with values of w ranging from 1.5 (momentum) to 3.0 (energy). Experimental data for low-velocity impacts (aluminum at 1 km s^{-1}) into medium-grained sand yield a value of $w = 2.53$ (Anderson *et al*., 2004).

Large spall fragments or incandescent ejecta clumps may allow tracking trajectories through time. The advance of the ejecta curtain (Figure 8) across the surface, however, will provide additional clues not just for the value of gravitational acceleration on the surface but also for inferences about target properties. Laser sheets used in 3D-PIV studies slice the ejection curtain and provide a unique view of the advancing wall of particles. Figure 9a shows the diameter of the ring of ejecta illuminated by the laser (8.9 cm above the pre-impact target surface) as a function of time after impact (t) scaled by the total time of crater formation (T). The diameter of the curtain (C_d) at any given time reflects where the ejecta left the surface (stage of growth), ejection angle, and ejection velocity. Consequently, C_d will not follow a simple relationship for different impact angles very early in crater growth but will converge at later times. For oblique impacts (30° and 60°), curtain diameter is taken transverse to the trajectory. Laser-illuminated ejecta in the curtain actually left the surface at an earlier stage of crater growth even when scaled time indicates that the crater has finished forming ($t/T \sim 1.0$) as described in Anderson *et al*. (2003).

The expansion velocity of the curtain with scaled time is shown in Figure 9b. Curtain velocity is now normalized to gravity-scaled ejecta velocity and reveals that this strategy accommodates a wide range of impact speeds and impact angles. The common relationship for very different experimental conditions reflects the horizontal velocity component of ballistic ejecta. At launch, ejecta speeds decrease with scaled time raised to an exponent of $-\gamma$ where $\gamma = 0.70$ for low-velocity impacts into sand. This exponent is higher for hypervelocity impacts when the projectile completely fragments at impact and approaches energy scaling (Schultz and Gault, 1983; Schultz, 1988). Curtain velocities progressively decrease with time but then increase after the crater finishes forming, as higher speed ejecta comprise the curtain at a given height above the surface. Values for a gravity-controlled 141 m-diameter crater produced by the DI collision are also shown in Figure 9b. Curtain

velocities decrease to about 30 cm s^{-1} at about one crater radius above the surface of the comet (in this case ~70 m) for the case of sand-like targets with gravity-controlled growth. Specific values on the ordinate to the right will increase by $2^{1/2}$ for a surface gravity twice as high. If gravity limits crater growth, the minimum outward curtain velocity will be greater when $t/T_c = 1$. Unusual target properties such as underdense materials (Figures 4–6) will affect specific values by increasing ejection angles and changing crater growth rates.

In gravity-controlled cratering, the expansion velocity of the ejecta curtain at the base initially decreases until the crater has finished forming since the curtain is tied to the growing cavity. Crater formation can be inferred when the ejecta curtain begins to make a sharp angle with the surface. At this time the curtain diameter at the base is about 25% larger than the final transient crater diameter. After crater

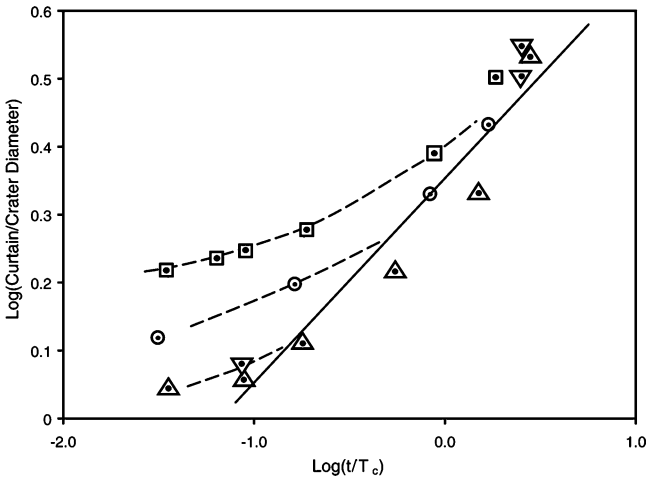

(a)

Figure 9. (a) Outward expansion of the ejecta curtain as a function of time (scaled by the total time for crater formation). Late-time expansion of the curtain for different impact conditions converge on a slope of 0.29 as expected for gravity-scaled growth. Early-time expansion of the curtain departs from expectations due to departure from a point source assumption and the effects of crater growth (ejecta launch angle from the surface). The following symbols apply for different impact conditions: 0.318 cm diameter aluminum spheres at ~5.5 km s^{-1} (circles for 90°; squares for 30°); 0.635 cm diameter spheres at ~1 km s^{-1} (upside-down triangle for 90°; triangles for 60°). (b) Outward curtain expansion speed observed in laboratory experiments for gravity-controlled growth. Speeds (ordinate to the right) for specific times (upper abscissa) are shown for the DI collision with the assumption of gravity-controlled crater scaling. Increase in growth after the crater has formed ($t/T = 1$) is due to the curtain being composed of faster ejecta launched from earlier times. If the comet is composed of weakly bonded grains, then the minimum observed velocity will be truncated. In both cases, height of the curtain is about 0.5 crater diameter (final) above the surface. Symbols are the same as in Figure 9a.

(*Continued on next page*)

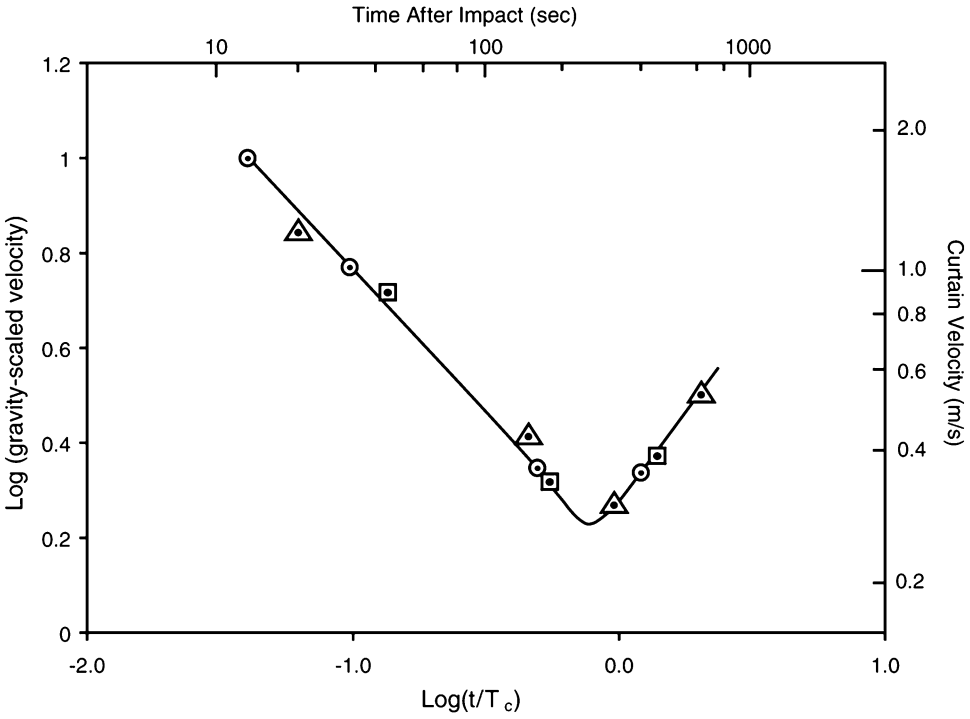

(b)

Figure 9. (*Continued*)

formation, the curtain diameter at the base progressively increases in velocity since the constituent ejecta were launched at higher velocities (e.g., Schultz and Gault, 1979). If strength limits crater growth, the ejecta curtain may detach from the crater (and perhaps even the comet).

Very high porosity targets will produce high ejection angles (60°) at late times in contrast with sand and pumice targets (45°–55°). Under-dense, compressible targets result in a two component, late-stage ejecta curtain (Figure 10): first, a vertical plume due to cavitation (temporary containment and redirection of vapor by the transient crater below the surface); second, an outward-moving curtain due to rarefaction-controlled excavation off the free surface. Figure 11a illustrates the vector-velocity field of particles within the curtain during ejection using the 3D-PIV technique for a loose sand target (see Anderson *et al.*, 2003, 2004). Figure 11b illustrates this velocity field for the ejecta curtain from a sieved perlite target. The gap in Figure 11b is due to fine (micron-size) debris within an opaque vertical plume that occults the laser beam used to image the slice through the ejecta curtain. In both examples, the ejecta have not been extrapolated back to the target surface. Figure 12 compares the final craters and the image slices for impacts into sand,

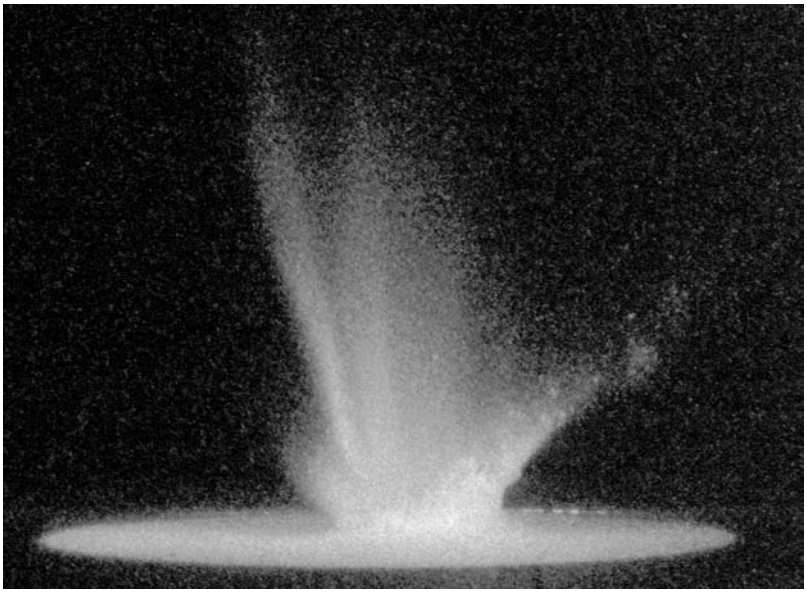

Figure 10. Impact into sieved perlite at 60° (0.318 cm diameter Pyrex sphere at ~5.6 km s^{-1}) results in a two-component ejecta plume at late stages: a high-angle plume due to deep penetration and an outward-advancing curtain related to shock rarefaction off the free surface. The high-angle plume gradually evolves as the cavity opens.

pumice, and perlite targets. At this stage of crater growth, the laser illuminates only the central, vertical plume of ejecta.

The third observable is the opacity of the curtain through time, which is related to both the evolving number density within the outward-advancing ejecta curtain and crater scaling. It is very unlikely that the ejecta curtain will form a uniform sheet as in experiments using a narrow range of particle sizes for the purposes of scaling relations. Instead, experiments using natural particulates demonstrate that the curtain forms clumps and gaps due to inhomogeneities in the target that evolve through time.

Theoretical and empirical models of ejecta curtain growth can be readily constructed from existing analytical models based on scaling theory or by extrapolating direct observations of the ejecta-mass velocity field, e.g., using data from 3D-PIV observations (see Anderson *et al.*, 2003, 2004). This technique provides simultaneous measurements of the evolution of the ejecta curtain dimensions (size and width), opacity, constituent ejection angles, and ejection velocities for a wide range of projectile and target properties. Even though gravity eventually limits crater growth, measured particle motions in the target beyond the rim allow assessing peak pressure decay and material flow affecting the potential growth at much lower gravity.

The fourth observable is the total brightening of the comet due to the sudden contribution of gas and dust into the coma. For sand targets, the total ejected mass is

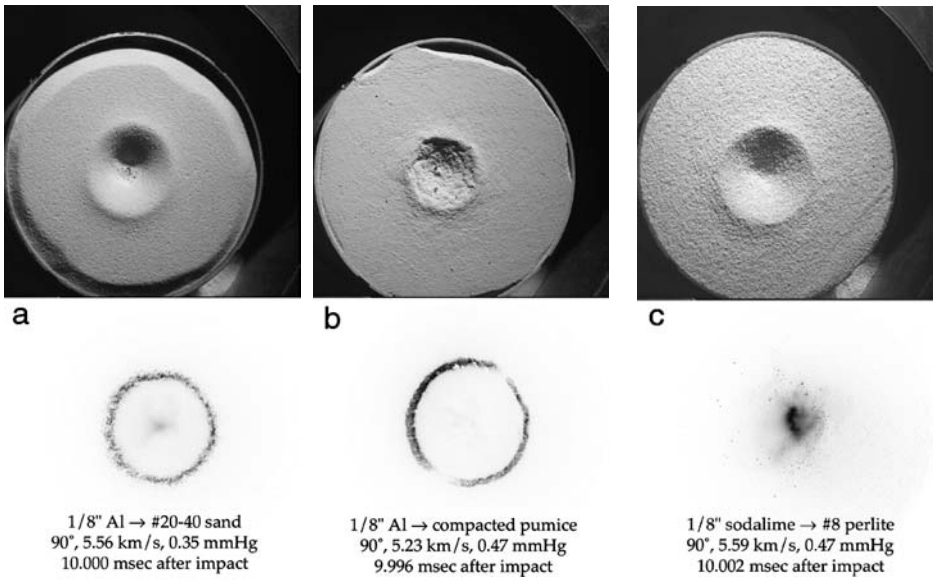

Figure 12. Comparison of final craters and ejecta illuminated by a laser sheet for sand (a), pumice (b), and perlite (c). The laser sheet illuminates individual ejecta particles as they pass through the plane. The illuminated individual grains have been reversed (black) in order to assist visualization. At any given time, ejecta from impacts into sand and pumice are confined within a narrow sheet (curtain) having a narrow range of velocities (see Figure 11a). The times correspond to dimensionless times of $\tau = 17512$ (12a), $\tau = 16{,}466$ (12b), and $\tau = 17610$ (12c). The central debris plume in Figure 12c is responsible for the split ejecta pattern in Figure 11b, as also shown in Figure 7a in quarter-space experiments. Note that the final crater in perlite appears only slightly larger than the crater in sand. This is the result of high-angle ejecta returning to the crater and the effect of rim collapse. Narrow band-pass filters minimized the effect of thermal radiation in the image.

about 50% of the total displaced mass shown in Figures 2 and 3. With the assumption of gravity-controlled growth as a reference, the DI impact could add 10^7–10^8 kg of dust and gas to the coma over the 3 to 6 min of crater formation. Late stages of ejection contain most of the mass but have low velocities (<10 m s^{-1}); consequently, the effect of this component will take hours to days to have a visible effect from Earth. For highly compressible targets (Figures 4–7), the total ejected mass may be reduced by a factor of 3 to 4 but may be collimated within a narrow cone (30° to 40° solid angle) in a region between the direction of the trajectory and the local surface normal.

5. Impact Radiation

5.1. Impact Flash

The emitted light energy from impacts is commonly termed the "impact flash", a term carried over from micro-particle experiments (e.g., Eichhorn, 1976) since the

duration is less than a microsecond. More recent studies using macroscopic projectiles (>500 μm) into porous silicate targets demonstrate, however, that this term is a misnomer because the radiation can last well over a millisecond (e.g., Ernst and Schultz, 2003). When scaled to the penetration time (Equation (6)), this represents a value of τ exceeding 1000. Light emissions can be characterized by two sources: atomic and molecular emissions from impact-generated vapor and blackbody radiation, whether from melt phases or vapor condensates. An extensive series of laboratory experiments are providing important clues for expectations for the Deep Impact collision. Despite the difference in scale, scaling relations for different substrate types (porous, easily volatized, competent) allow first-order extrapolations. The goal here is to estimate the intensity evolution and character (color temperature, peak intensity, decay) as a function of substrate type and impact angle in order to understand the underlying causes (or at least limit the possibilities) for the final crater appearance. The detailed view of light emissions from laboratory experiments will not be resolved fully by either spacecraft or earth-based instruments. But understanding the underlying causes for observed light emission requires such details. Consequently we first review expectations for the total visible and near infrared emissions.

5.2. Integrated Luminous Intensity

For a purely kinetic event (kinetic energy transferred to luminous energy), the Stefan-Boltzmann relation requires the following for the radiance, R, at the source for condensed phase radiation:

$$R = \sigma T^4 \tag{9}$$

where total radiance is in W m^{-2}; σ is the Stephan-Boltzmann constant (5.67×10^{-8} W m^{-2} K^{-4}); and T is the color temperature (K). The total luminous energy, LE, is then:

$$\mathrm{LE} = (\sigma T^4)(A_s \Delta t) \tag{10}$$

where A_s represents the effective source area and Δt is the duration of the emissions. More accurately, LE should be written as:

$$\begin{aligned} \mathrm{LE}(\theta) &= \int_0^t \mathrm{LE}(\theta, t)\, dt \\ &= \sigma \int_0^t T_\theta^4 A_\theta\, dt \end{aligned} \tag{11}$$

where the radiating source color temperature and area vary with time for a given impact angle (θ) and target.

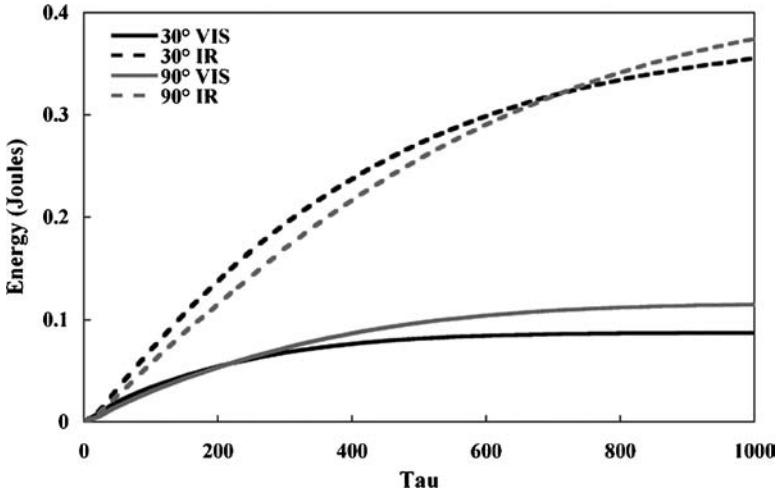

Figure 13. Observed cumulative radiant energy for hypervelocity impacts (5.5 km s^{-1}) into pumice at 90° and 30° in laboratory experiments. Radiant energy is calculated from the observed blackbody (color) temperature and source area through time. The evolution of the radiant energy in the visible (0.34 to 1.0 μm) and infrared (1.0 to 4.8 μm) is shown.

Various studies (Melosh *et al.*, 1993; Nemtchinov *et al.*, 1999, 2000; Artm'eva *et al.*, 2000) suggest that LE can be expressed as a fraction of the kinetic energy of the impact (KE_i):

$$LE = \eta \cdot KE_i . \tag{12}$$

Previous estimates suggested that η (the luminous efficiency) might range from 10^{-5} to 10^{-6} depending on the target. These efficiencies are based on gas phase radiation and are consistent with direct measurements of efficiencies in the laboratory (Sugita *et al.*, 2003).

Hypervelocity impacts into silicate targets (velocities of 5 to 6 km s^{-1}), however, indicate a much higher total (all wavelengths) luminous efficiency of 10^{-4} to 10^{-3}. Observations of color temperature and radiating source area through time (see Ernst and Schultz, 2004) allow integrating Equation (11) to give the cumulative radiant energy with dimensionless time, τ, for 90° (vertical) and 30° impacts into pumice at around 5.6 km s^{-1} as shown in Figure 13. Here the radiant energy is shown only for the wavelength ranges of interest to the DI instruments for the visible CCD (0.34 to 1.0 μm) and the infrared spectrometer (1.0 to 4.8 μm). The total integrated radiant flux for all wavelengths represent about 0.7 joules over $\tau = 1000$, which represents a luminous efficiency of about 3.5×10^{-4} largely due to heated silicates that incandesce long after first contact.

If the light energy is a simple fraction of the impact energy for a given target, then Equation (12) requires that $(R \cdot A_s \cdot \Delta t)$ is proportional to impact energy as well. Each of the independent variables (color temperature, area, and duration) can be directly

related in laboratory impact experiments in order to test the assumption that η is approximately constant for a given target. Such measurements are part of an ongoing experimental study for the radiation from the thermal (Ernst and Schultz, 2002, 2003, 2004) and atomic/molecular emission lines (Sugita and Schultz, 1999; Sugita *et al.*, 1998; Sugita and Schultz, 2003a, b; Eberhardy and Schultz, 2003, 2004).

For purposes here, it is assumed that the laboratory experimental results can be used to derive the color temperature, source area, and duration as a function of impactor size and velocity. This approach strictly applies only to the silicate targets used in these experiments. The rationale for using silicates is that minimal vaporization occurs at the available impact velocities, thereby minimizing the complicating effect of phase changes and energy expended in atomic/molecular transitions. The possible effect of volatile-rich components is discussed below.

Experiments indicate that the peak radiant flux is proportional to v^{ω} where $\omega \sim 5.5$ (see Ernst and Schultz, 2002; 2003). Such a strong dependence on impact velocity seems counterintuitive but the same relation is found for atomic-emission line intensity (Sugita *et al.*, 1998). After the initial peak intensity decays, the experimental ω approaches 3, a value consistent with conservation of energy (see Schultz *et al.*, 2004). This also can be expressed as $T \sim v^{0.75}$. Consequently, the integrated radiant flux for DI (LE_{DI}) relative to the laboratory experiments (LE_L) is given by:

$$\frac{\mathrm{LE_{DI}}}{\mathrm{LE}_L} \sim \left(\frac{T_{\mathrm{DI}}}{T_L}\right)^4 \left(\frac{A_{\mathrm{DI}}}{A_L}\right)\left(\frac{\Delta t_L}{\Delta t_{\mathrm{DI}}}\right) \sim \left(\frac{a_L}{a_{\mathrm{DI}}}\right)^3 \left(\frac{v_{\mathrm{DI}}}{v_L}\right)^2. \tag{13}$$

The projectile ratio of about $(90/0.476)^3$ and velocity ratio of $(10.2/5.5)^2$ would indicate an integrated radiance approximately 2.3×10^7 times that observed in the laboratory experiments. This would scale to a total of about 15 MJ of light energy for the DI collision (luminous efficiency of $\sim 0.08\%$). Such a thermal plume could last more than 60 ms.

Experiments indicate that the luminous efficiency could be almost an order of magnitude greater for a silicate-rich, particulate target. Conceivably, it could increase to 6th magnitude, depending on the duration and visibility (e.g., view angle). Figure 14 provides results of a more complete extrapolation where the temperature and source area are scaled to the DI collision and integrated over time for the visible camera and the infrared spectrometer. The sampling rate of the MRI is about 0.06 s at the time of impact. Consequently, the event might be captured in only one or two frames. It also could extend over 10–50 frames if the comet surface contains a particulate silicate-rich surface.

The estimates for the radiant energy (apparent magnitude) and duration depend on several important factors. First, the porosity of the target dramatically affects the peak intensity, decay, and duration (Ernst and Schultz, 2003). Highly porous particulate targets (such as sieved perlite used in laboratory experiments) produce a peak intensity reduced by half and a duration shortened by more than two orders of magnitude. Second, the nature of the target (e.g., solid pumice vs. particulate

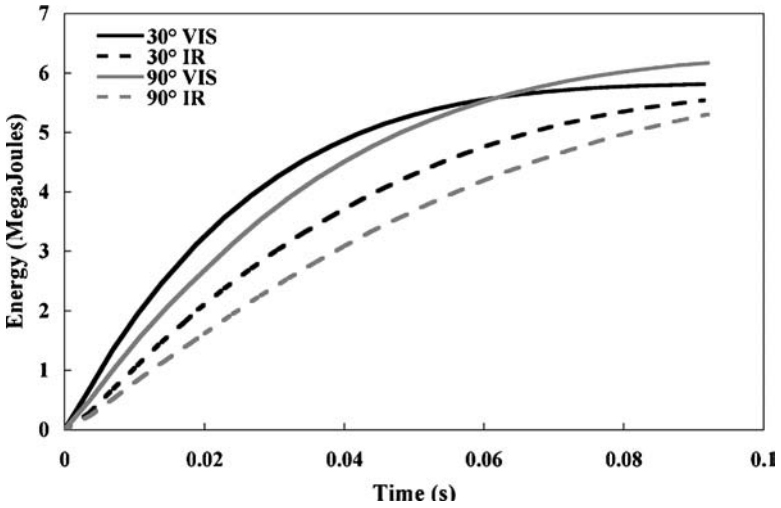

Figure 14. Observed cumulative radiant energy extrapolated from observations of color temperature and radiating source area in laboratory experiments (Figure 13) to the Deep Impact collision as discussed in the text.

pumice) also reduces the peak intensity by half and duration by a factor of two. Third, the target volatile content dramatically affects the blackbody radiation responsible for the longer duration radiation. The greater volatile content results in greater radiant energy represented in emission lines over limited wavelengths. Such sources are subject to the issues of self-absorption, ionization, and optical depth (see Sugita and Schultz, 2003a, b; Sugita *et al*., 2003), thereby complicating unique interpretations of this component by the available DI instruments. Fourth, interactions between DI ejecta and the surrounding coma gas may create secondary radiation sources, thereby enhancing and prolonging the inferred luminosity and duration greatly (e.g., Sugita and Schultz, 2003a). In spite of such caveats, the ongoing laboratory experiments provide key strategies for using various instruments to interpret the nature of the impacted substrate, particularly if the crater is unexpectedly small.

6. Concluding Remarks

The Deep Impact "hard" encounter represents a unique large-scale experiment. In laboratory experiments, all independent variables are controlled. For the Deep Impact experiment, the composition, structure, density (porosity), gravity, and impact angle are not known or will not be well constrained until after the impact. Nevertheless, results of laboratory experiments allow predictions for the DI event:

1.) Smaller than expected crater (<50 m in diameter)

a.) If the crater is smaller than predicted due to post-shock surface strength (SC model), then the crater will nevertheless be deep due to the anticipated low density (<0.5 g cm^{-3}) that allows deep penetration. The ejecta plume will initially expand spherically above the target, followed by a vertical, high-temperature plume (see Figure 15). Spall fragments will dominate late-stage excavation; a well-defined ejecta curtain will not develop. The flash will be very short (several frames in the MRI).

b.) Large pockets (1 to 10 m) of highly porous (>80%) and compressible material embedded in a matrix of fine particulates could reduce the coupling of the initial shock to the comet. The weak shock front then might not overcome the interparticle binding forces in the matrix or frictional drag could arrest growth before achieving the gravity limit.

c.) The high encounter velocity still should induce catastrophic disruption of the DI probe during entry and result in a large transient crater. An extremely

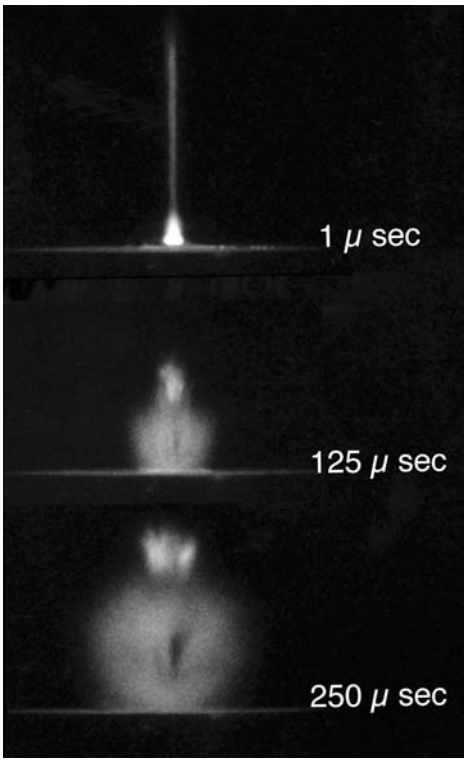

Figure 15. Vertical impact by a 0.635 cm diameter pyrex sphere into dry ice (side view) at 5.4 km s^{-1} under near-vacuum conditions. In the first frame a high–velocity jet-like spike is directed out of the small penetration opening. This "jet" is actually a parcel of hot gas that is smeared in the first frame due to its high velocity (∼3 km s^{-1}). A spherical cloud of CO and CO_2 vapor expands above the impact followed by a high-temperature plume that "blooms" above the spherical plume after 125 μs.

high porosity (80%) and compressibility, however, may produce a final crater that is unexpectedly smaller primarily due to wall collapse of the transient cavity, even at $g = 0.04\,\mathrm{cm\,s^{-2}}$. In this scenario (and in Scenario 1b), a three-component plume should be observed in the MRI and may allow the identification of this surface property.

i. $T = 0.06$ s (first frame): very weak flash.
ii. $T = 1$ s ($\sim$17 frames): high-angle jet-like plasma plume due to cavitation and redirection back out the penetration funnel.
iii. $T = 1$ to 20 s: opaque spherical cloud forming a shadow above the comet surface.
iv. $T = 20$ s to 100 s: high-angle ejecta plume extending >10 km above the surface surrounded by a high-angle ($\sim 60^\circ$) ejecta curtain.
v. $T > 200$ s: advancing annulus of disturbed cometary surface near the crater as low-velocity components return. High-angle central plume may detach from the crater due to collapse and shut off of deep ejecta.

2.) Nominal crater dimensions ($\sim$80 to 130 m)

a.) A crater produced in a lunar regolith-like material (PR model) should grow with a final diameter:depth (rim-to-floor) ratio of 4:1 to 5:1.
b.) If the near-surface material is volatile-rich (silicate poor), a well-defined ejecta curtain will be delayed until very late time ($\sim$100 s). The flash will be weak and dominated by atomic and molecular emission lines with little blackbody until solid condensates form. Strong absorptions may develop as cooler gases expand in front of the thermal background.
c.) If the near-surface material is silicate rich (volatile poor), a well-defined ejecta curtain will evolve as in laboratory experiments. The flash will be largely thermal and of long duration (up to 1 s) as ejecta fragments cool. A strong thermal source will remain on the crater floor but cooling melt breccias (1 to 10 cm) may be traced to large distances in the IR.

3.) Larger than expected (>180 m)

a.) Backpressures created by vapor expansion may augment crater growth, particularly if deep penetration occurs. Exothermic reactions also may contribute if metastable components (C, H, N, O) at cold conditions react under high temperatures or if latent heat is released at depth due to phase changes. The classic ejecta curtain may not develop due to rapid expansion and dissipation of the vapor phases. The crater may continue to "feed" volatiles to the coma as the thermal wave penetrates more deeply into the comet.
b.) Extremely low density cometary surface ($0.1\,\mathrm{g\,cm^{-3}}$ down to a depth of <50 m depth) could produce a much larger than expected crater since cratering efficiency reflects mass, not volume (UR model). The evolution

of the ejecta plume and curtain (direct or in shadow) would follow Scenario 1b.

4.) Craters in composite or layered surface materials (CL model)

a.) A layered comet structure with weak, low-density surface (1–10 m deep) over a competent layer would result in a large but shallow crater with a central penetration pit. The diameter of the outer crater would depend on $(\delta_p/\delta_t)^{1/3}$ of the surface layer. A two-component ejecta curtain should be evident: a vertical plume surrounded by a thin (less opaque) advancing curtain.

b.) A layered comet structure with a strong surface layer over a low-density substrate would result in an irregularly shaped crater with radial and concentric fractures, large ejecta spalls and rayed ejecta. The crater rim would be very ill defined and bulbous due to under-thrusting and upward displacement followed by collapse.

The qualitative predictions above represent a combination of direct observations from laboratory experiments and the morphology of small ($<$100 m) craters on the lunar surface (e.g., Schultz, 1976). The wide range in alternative scenarios underscores the fact that the results of this mission will provide a new understanding of not only comet properties but also key physical processes related to impact cratering at a much larger scale and higher impact velocities.

Acknowledgments

The authors gratefully acknowledge the professional assistance by the technical crew (D. Holt, D. Bowling, R. Smythe, and C. Cornelison) at the NASA Ames Vertical Gun Range, funded through the Planetary Geophysics Program, Office of Space Science, and NASA Headquarters. The research was made possible by support from NASA's Deep Impact Discovery mission, managed through the University of Maryland and Michael A'Hearn. The authors also gratefully acknowledge the assistance of J. T. Heineck for the 3D-PIV data presented here, as well as fruitful discussions with Seiji Sugita.

References

Adams, M. A., Schultz, P. H., Sugita, S., and Goguen, J. D.: 1997, *Lunar Planet. Sci. XXVIII*, Abstract, p. 3.

A'Hearn, M., Belton, M. J. S., Delamere, A., and Blume, W. H.: 2005, Space Science Reviews (this volume).

Anderson, J. L. B., Schultz, P. H., and Heineck, J. T.: 2003, *J. Geophys. Res.* **108**, E8, doi:10.1029/2003JE002075.

Anderson, J. L. B., Schultz, P. H., and Heineck, J. T.: 2004, *Meteor. Planet. Sci.* **39**, 303.

Artem'eva, N. A., Kosarev, I. B. V., Nemchinov, I., Trubetskaya, I. A., and Shuvalov, V. V.: 2000, *Solar System Res.* **34**, 453.
Boslough, M. B., Crawford, D. A., Robinson, A. C., and Trucano, T. G.: 1994, *Geophys. Res. Lett*. **21**, 1555.
Brownlee, D. E. *et al*.: 2004, *Science* **304**, 1764.
Chabai, A. J.: 1977, in Roddy, D. J., Pepin, R. O., and Merrill, R. B. (eds.), *Impact and Explosion Cratering*, Pergamon Press, New York, p. 1191.
Chapman, C. R. and McKinnon, W. B.: 1986, in Burns, J. A. and Matthews, M. S. (eds.), *Satellites*, University of Arizona Press, Tucson, p. 492.
Cintala, M. J., Berthoud, L., and Hörz, F.: 1999, *Meteor. Planet. Sci*. **34**, 605.
Dahl, J. M. and Schultz, P. H.: 1999, *Lunar Planet Sci. XXX*, LPI, Abstract No. 1854.
Dahl, J. M. and Schultz, P. H.: 2001, *Internat. J. Impact Engin*. **26**, 145.
Dienes, J. K. and Walsh, J. M.: 1970, in Kinslow, R. (ed.), *Hypervelocity Impact Phenomena*, Academic Press, New York, p. 45.
Eichhorn, G.: 1976, *Planet. Space Sci*. **24**, 771.
Eberhardy, C. A. and Schultz, P. H.: 2003, *Lunar Planet. Sci. Conf. XXXIV*, Abstract No. 1855.
Eberhardy, C. A. and Schultz, P. H.: 2004, *Lunar Planet. Sci. Conf. XXXV*, Abstract No. 2039.
Ernst, C. M. and Schultz, P. H.: 2002, *Lunar Planet. Sci. Conf. XXXIII*, Abstract No. 1782.
Ernst, C. M. and Schultz, P. H.: 2003. *Lunar Planet. Sci. Conf. XXXIV*, Abstract No. 2020.
Ernst, C. M. and Schultz, P. H.: 2004, *Lunar Planet. Sci. Conf. XXXV*, Abstract No.1721.
Gault, D. E. and Wedekind, J. A.: 1977, in Roddy, D. J., Pepin, R. O. and Merrill, R. B. (eds.), *Impact and Explosion Cratering*, Pergamon Press, New York, p. 1231
Gault, D. E. and Wedekind, J. A.: 1978, *Proceedings Lunar Planet. Sci. Conf. 9th*, 3843.
Gault, D. E., Quaide, W. L., and Oberbeck, V. R.: 1968, in French, B. M. and Short, N. M. (eds.), *Shock Metamorphism of Natural Materials*, Mono Books, San Francisco, p. 87.
Gault, D. E., Guest, J. E., Murray, J. B., Dzurisin, D., and Malin M. C.: 1975, *J. Geophys. Res.* **80**, 2444.
Holsapple, K. A.: 1987, *Int. J. Impact Engin.* **5**, 343.
Holsapple, K. A. and Schmidt, R. M.: 1982, *J. Geophys. Res*. **87**, 1849.
Holsapple, K. A. and Schmidt, R. M.: 1987, *J. Geophys. Res*. **92**, 6350.
Housen, K. R., Schmidt, R. M., and Holsapple, K. A.: 1983, *J. Geophys. Res*. **88**, 2485.
Housen, K. R., Holsapple, K. A., and Voss, M. E.: 1999, *Nature*. **402**, 155.
Melosh, H. J., Artemieva, N. A., Golub, A. P., Nemtchinov, I. V., Shuvalov, V. V., and Trubetskaya, I. A.: 1993, *Lunar Planet. Sci. Conf. XXIV*, 975.
Nemtchinov, I. V., Shuvalov, V. V., Artemieva, N. A., Kosarev, I. B., and Trubetskaya, I. A.: 1999, *Int. J. Impact Engin.* **23**, 651.
Nemtchinov, I. V., Spalding, R. E., Shuvalov, V. V., Artem'eva, N. A., Kosarev, I. B., and Popel, S. I.: 2000, *Lunar Planet. Sci. Conf*. XXXI, Abstract No. 1334.
O'Keefe, J. D. and Ahrens, T. J.: 1977, *Lunar Planet. Sci. Conf*. VIII, 3357.
O'Keefe, J. D., Stewart, S. T., and Ahrens, T. J.: 2002, *Lunar and Planet Sci. XXXIII*, Abstract No. 2002.
Orphal, D. L.: 1977, in Roddy, D. J., Pepin, R. O., and Merrill, R. B., (eds.), *Impact and Explosion Cratering: Overviews*, Pergamon Press, New York, p. 907.
Piekutowski, A. J.: 1977, in Roddy, D. J., Pepin, R. O. and Merrill, R. B. (eds.), *Impact and Explosion Cratering*, Pergamon Press, New York, p. 67.
Post, R. L.: 1974, *Rep. AFWL-TR-74-51*, Air Force Weapons Lab, Kirtland, AFB, N. M.
Quaide, W. L. and Oberbeck, V. R.: 1968, *J. Geophys. Res*. **73**, 5247.
Schmidt, R. M.: 1980, *Proc Lunar Planetary Science Conference XI*, 2099.
Schmidt, R. M.: 1977, in Roddy, D. J., Pepin, R. O., and Merrill, R. B. (eds.), *Impact and Explosion Cratering: Overviews*, Pergamon Press, New York, p. 1261.

Schmidt, R. M. and Holsapple, K. A.: 1982, in Silver, L. T. and Schultz, P. H. (eds.), *Geological Implications of Impacts of Large Asteroids and Comets on the Earth*, Geological Society of America Special Paper, p. 93.
Schmidt, R. M. and Housen, K. R.: 1987, *Int. J. Impact Eng*. **5**, 543.
Schultz, P. H.: 1976, *Moon Morphology*: *Interpretations Based on Lunar Orbiter Photography*, University of Texas Press, Austin, 626 pp.
Schultz, P. H.: 1988, in Vilas, F., Chapman, C., and Mathews, M. (eds.), *Mercury*, University of Arizona Press, Tucson, p. 274.
Schultz, P. H.: 1992, *J. Geophys. Res*. **97(E10)**, 16,183.
Schultz, P. H.: 1996, *J. Geophys. Res*.**101(E9)**, 21,117.
Schultz, P. H., Adams, M. A., Perry, J. W., and Goguen, J.: 1996, *Lunar Planet. Sci. Conf. XXVII*, Abstract, p. 1149.
Schultz, P. H.: 2000, *Lunar Planet. Sci. Conf*. XXXI, Abstract No. 2071.
Schultz, P. H.: 2001, *Bull. Am. Astron. Soc.* **33**, 1095.
Schultz, P. H.: 2003a, *Lunar Planet. Sci. Conf*. XXXIV, Abstract No. 2067.
Schultz, P. H.: 2003b, *Sixth International Conference on Mars*, Abstract No. 3263.
Schultz, P. H. and Gault, D. E.: 1979, *J. Geophys. Res*. **84**, 7669.
Schultz, P. H. and Gault, D. E.: 1983, *Lunar and Planet. Sci. XV*, Abstract, p. 730.
Schultz, P. H. and Gault, D. E.: 1985a, *J. Geophys. Res.* **90**, 3701.
Schultz, P. H. and Gault, D. E.: 1985b, *Lunar and Planet. Sci. XVI*, Abstract, p. 742.
Schultz, P. H. and Gault, D. E.: 1990, in Silver, L. and Schultz, P. (eds.), *Geological Implications of Impacts of Large Asteroids and Comets on the Earth*, Geol. Society of Amer. Spec. Paper. 247, p. 239.
Schultz, P. H., Orphal, D., Miller, B., Borden, W. F., and Larson, S. A.: 1981, in Merrill, R. B. and Schultz, P. H., (eds.), *Proceedings of the Conference on Multi-Ring Basins: Formation and Evolution*, Pergamon Press, New York, p. 181.
Schultz, P. H., Anderson, J. L. B., and Heineck, J. T.: 2002, *Lunar Planet. Sci. Conf. XXXIII*, Abstract No. 1875.
Schultz, P. H., Sugita, S., Eberhardy, C. A., and Ernst, C. M.: 2004, *Lunar Planet. Sci. Conf. XXXV*, Abstract No. 1946.
Soderblom, L. A., *et al*.: 2002, Science **296**, 1087.
Stöffler, D., Gault, D. E., Wedekind, J., and Polkowski, G.: 1975, *J. Geophys. Res.* **80**, 4062.
Sugita, S., Schultz, P. H., and Adams, M. A.: 1998, *J. Geophys. Res*. **103(E8)**, 19,427.
Sugita, S. and Schultz, P. H.: 1999, *J. Geophys. Res*. **104(E12)**, 30,825.
Sugita, S. and Schultz, P. H.: 2003a, *J. Geophys. Res*. **108(E6)**, 5152, doi: 10.1029/2002JE001960.
Sugita, S. and Schultz, P. H.: 2003b, *J. Geophys. Res*. **108(E6)**, 5151, doi: 10.1029/2002JE001959.
Sugita, S., Schultz, P. H., and Hasegawa, S.: 2003, *J. Geophys. Res.* **108(E12)**, 5140, doi:10.1029/2003JE002156.